

Photometry and Spectroscopy of GRB 060526: A detailed study of the afterglow and host of a high-redshift gamma-ray burst

C. C. Thöne¹, D. A. Kann², G. Jóhannesson^{3,4}, J. H. Selj⁵, A. Jaunsen⁵, J. P. U. Fynbo¹, K. S. Baliyan⁶, C. Bartolini⁷, I. F. Bikmaev⁸, J. S. Bloom⁹, R. A. Burenin¹⁰, B. E. Cobb¹¹, S. Covino¹², P. A. Curran¹³, H. Dahle⁵, J. French¹⁴, S. Ganesh⁶, G. Greco⁷, A. Guarnieri⁷, L. Hanlon¹⁴, J. Hjorth¹, M. Ibrahimov¹⁵, G. L. Israel¹⁶, P. Jakobsson¹⁷, B. L. Jensen¹, U. G. Jørgensen¹⁸, I. M. Khamitov¹⁹, D. Malesani¹, N. Masetti²⁰, J. Näränen²¹, E. Pakstiene²², M. N. Pavlinsky¹⁰, D. A. Perley⁹, A. Piccioni⁷, G. Pizzichini²⁰, A. Pozanenko¹⁰, D. Nanni¹⁶, V. Romyantsev²³, D. Sharapov¹⁵, D. Star⁹, R. A. Sunyaev^{10,24}, F. Terra²⁵, P. M. Vreeswijk¹, and A. C. Wilson²⁶

¹ Dark Cosmology Centre, Niels Bohr Institute, University of Copenhagen, Juliane Maries Vej 30, 2100 Copenhagen, Denmark
e-mail: cthoene@dark-cosmology.dk

² Thüringer Landessternwarte Tautenburg, Sternwarte 5, 07778 Tautenburg, Germany

³ Science Institute, University of Iceland, Dunhaga 3, 107 Reykjavík, Iceland

⁴ Hansen Experimental Physics Laboratory, Stanford University, Stanford, CA 94305

⁵ Institute of Theoretical Astrophysics, University of Oslo, P.O. Box 1029 Blindern, N-0315 Oslo, Norway

⁶ Physical Research Laboratory, Ahmedabad-380 009, India

⁷ Dipartimento di Astronomia, Università di Bologna, via Ranzani 1, 40127 Bologna, Italy

⁸ Kazan State University and Academy of Sciences of Tatarstan, Kazan, Russia

⁹ Department of Astronomy, 601 Campbell Hall, University of California, Berkeley, CA 94720-3411

¹⁰ Space Research Institute (IKI), 84/32 Profsoyuznaya Str, Moscow 117997, Russia

¹¹ Department of Astronomy, Yale University, P.O. Box 208101, New Haven, CT 06520

¹² INAF - Osservatorio Astronomico di Brera, via Bianchi 46, 23807 Merate (Lc), Italy

¹³ Astronomical Institute “Anton Pannekoek”, University of Amsterdam, Kruislaan 403, 1098 SJ Amsterdam, The Netherlands

¹⁴ UCD School of Physics, University College Dublin, Belfield, Dublin 4, Ireland

¹⁵ Ulugh Beg Astronomical Institute, 33 Astronomical Str., Tashkent 700052, Uzbekistan

¹⁶ INAF-Osservatorio Astronomico di Roma, Via Frascati 33, 00040 Monteporzio Catone, Italy

¹⁷ Centre for Astrophysics Research, University of Hertfordshire, College Lane, Hatfield, Herts, AL10 9AB, UK

¹⁸ Niels Bohr Institute, University of Copenhagen, Juliane Maries Vej 30, 2100 Copenhagen, Denmark

¹⁹ TUBITAK National Observatory, Antalya, Turkey

²⁰ INAF - Istituto di Astrofisica Spaziale e Fisica Cosmica di Bologna, Via Gobetti 101, 40129 Bologna, Italy

²¹ University of Helsinki Observatory, P.O. Box 14 (Tähtitorninmäki), 00014, Finland

²² VU Institute of Theoretical Physics and Astronomy, A. Gostauto 12, 01108 Vilnius, Lithuania

²³ Crimean Astrophysical Observatory, Nauchny, Crimea, 98409, Ukraine

²⁴ Max-Planck-Institut für Astrophysik, Karl-Schwarzschild Straße 1, 85741 Garching, Germany

²⁵ Second University of Roma “Tor Vergata”, Italy

²⁶ Department of Astronomy, University of Texas at Austin, Austin TX, 78712

Received; accepted

ABSTRACT

Aims. With this paper we want to investigate the highly variable afterglow light curve and environment of Gamma-Ray Burst (GRB) 060526 at $z=3.221$.

Methods. We present one of the largest photometric datasets ever obtained for a GRB afterglow, consisting of multi-color photometric data from the optical to the NIR. The data set contains 218 data points in total to which we add additional data from the literature. Furthermore, we present low-resolution high signal-to-noise spectra of the afterglow. The afterglow light curve is modeled with both an analytical model using broken power-law fits and with a broadband numerical energy injection model. The absorption lines detected in the spectra are used to derive column densities using a multi-ion single-component curve-of-growth analysis from which we derive the metallicity of the host of GRB 060526.

Results. The overall light curve follows a broken power-law with a break at $t = 2.401 \pm 0.061$ days. It shows deviations from the smooth power-law that can be explained by additional energy injections from the central engine. The broadband SED of the afterglow shows little extinction along the line of sight. The metallicity derived from S II and Fe II is relatively high for a galaxy at that redshift but comparable to the metallicity of other GRB hosts at similar redshifts. There is a candidate host galaxy at a relatively large offset of 7.7 kpc from the afterglow position with $R = 26.4$ mag which would imply a rather luminous host.

Key words. gamma rays: bursts – gamma rays bursts: individual: GRB 060526 – galaxies: high redshift – interstellar medium: abundances

1. Introduction

Gamma-Ray Bursts (GRBs) and their afterglows offer a powerful tool to probe the high-redshift universe, both through photometry and spectroscopy (e.g. Prochaska et al., 2006). The standard fireball model of GRB afterglows (see Zhang, 2007; Mészáros et al., 2006, for recent reviews on the topic) predicts a smooth temporal evolution which can be empirically described by a smoothly joint broken power-law, the so-called Beuermann equation (Beuermann et al., 1999). In many cases, when temporally dense afterglow photometry was obtained, the afterglow evolution was found to be smooth as, e.g., in GRB 020813 (Laursen & Stanek, 2003), GRB 030226 (Klose et al., 2004) and GRB 041006 (Stanek et al., 2005) (for the complete pre-*Swift* sample see Zeh et al., 2006). Out of the total sample of 59 afterglows of that paper, only four of the GRBs analysed showed significant deviations from the expected decay (though we note that about half of the 59 afterglows were not sampled well enough to allow any conclusions). Two of these might be explained by microlensing (GRB 000301C, Garnavich et al., 2000) or an inhomogeneous emitting surface (GRB 011211, Jakobsson et al., 2004). The only two GRBs which showed long-lasting strong deviations are GRB 021004 (e.g. de Ugarte Postigo et al., 2005, and references therein) and GRB 030329 (e.g. Lipkin et al., 2004, and references therein) which incidentally also have the densest optical monitoring.

With the launch of the *Swift* satellite and its rapid localization capabilities (Gehrels et al., 2004), the number of highly variable light curves has increased considerably. Examples are small, achromatic bumps overlying the smooth power-law decay (e.g., GRB 050502A, Guidorzi et al. 2005; GRB 061007, Mundell et al. 2007), early bumps with chromatic evolution (e.g., GRB 061126, Perley et al. 2008a; GRB 071003, Perley et al. 2008b), “steps” due to energy injection episodes (e.g., GRB 070125, Urdike et al. 2008; GRB 071010A, Covino et al. 2008) or powerful late-time rebrightenings of up to several magnitudes (e.g., GRB 050721, Antonelli et al. 2006; GRB 060206, Woźniak et al. 2006; Monfardini et al. 2006; Stanek et al. 2007; GRB 070311, Guidorzi et al. 2007; GRB 071003, Perley et al. 2008b). The early time domain, which can now be routinely accessed by rapid follow-up in the *Swift* era, has yielded more types of variability, like rising afterglows (e.g., GRB 060418, Molinari et al. 2007; GRB 060605, Ferrero et al. 2008; GRB 060607A, Nysewander et al. 2007) and short-term variability directly linked to the prompt emission (e.g., GRB 041219A, Vestrand et al. 2005; Blake et al. 2005; GRB 050820A, Vestrand et al. 2006; GRB 080319B, Racusin et al. 2008). In all these cases, dense photometric follow-up during the periods of variability was needed to characterize the phenomena involved.

GRB afterglows can in addition be used to study their galactic environment through absorption line spectroscopy of material in the line-of-sight towards the GRB. Above a redshift of around $z \sim 0.2$, resonant absorption lines from elements present in the interstellar medium (ISM) such as Mg, Zn, Fe, Si, C, and S are shifted into the optical regime and can be studied with ground-based telescopes. For 10 bursts between a redshift of $z = 2$ to 6, the metallicity along the line-of-sight in the galaxy could be obtained so far (e.g. Savaglio, 2006; Fynbo et al., 2006; Price et al., 2007, and references therein). The values are usually below solar, but higher than for QSO absorbers at comparable redshifts, some of them even higher than theoretical limits for the formation of collapsars (Woosley & Heger, 2006). The dif-

ference to QSO absorbers can be explained if GRB sightlines probe denser parts of the galaxy, or if GRBs reside in galaxies with higher masses and therefore higher metallicities. Both for QSO and GRB absorbers, there is a metallicity evolution with redshift (Savaglio, 2006; Fynbo et al., 2006; Price et al., 2007), although the slope is different for the two samples. GRB hosts seem to show a low extinction along the line-of-sight (Prochaska et al., 2007), however, relative abundances of heavier elements indicate that some of the ions must be depleted onto dust grains and the depletion pattern resembles the one found in the warm disc and halo of the Milky Way (MW) (Savaglio, 2006). How this can be explained together with the low extinction as also derived from the spectral energy distribution (SED) of the afterglow (Kann et al., 2006; Starling et al., 2007; Kann et al., 2007), is still an open question. One possible solution to this problem is destruction of the dust present in the line-of-sight by the GRB and afterglow radiation (e.g., Waxman & Draine, 2000).

GRB 060526 was detected by the *Swift* satellite on May 26.686458 (16:28:30 UT). The satellite slewed immediately to the burst, detecting both the X-ray and the optical afterglow (Campana et al., 2006a). The BAT instrument on *Swift* measured two emission epochs. The first one lasted 13.8 s and consisted of two FRED peaks, followed by a second symmetric peak between 230 to 270 s (Campana et al., 2006b). The second peak was coincident with a giant X-ray flare followed by a softer flare at 310 s (Campana et al., 2006c) also detected in the V-band by the UVOT telescope onboard *Swift* (Brown et al., 2006). The gamma-ray fluence was $4.9 \pm 0.6 \times 10^{-7}$ erg/cm² during the first emission episode and $5.9 \pm 0.6 \times 10^{-7}$ erg/cm² during the second, the peak flux of the second episode was however only half of the peak flux of the first one. The spectral index of the two epochs changed from 1.66 ± 0.20 to 2.07 ± 0.18 , thus showing the typical hard-to-soft evolution (Markwardt et al., 2006). The most rapid ground-based observations came from *Watcher*, which detected the afterglow at $R \approx 15$ mag (French & Jélinek, 2006) 36.2 seconds after the trigger. *ROTSE* observations showed a plateau for several thousand seconds after the GRB (Rykoﬀ et al., 2006). A redshift of $z = 3.21$ was determined by Berger & Gladders (2006) with the Magellan/Clay telescope. The brightness of the optical afterglow allowed for a dense monitoring which revealed a complex light curve structure including several flares (Halpern et al., 2006a,b) and a steepening attributed to a jet break (Thöne et al., 2006).

In this paper, we approach the analysis of GRB 060526 from two sides: Through modelling of the very detailed optical light curve and late optical imaging of the field to detect the host in Sec. 3, and analysis of low to medium resolution spectroscopic observations of absorption lines along the line of sight (Sec. 4). Throughout the paper, we follow the convention $F_\nu(t) \propto t^{-\alpha} \nu^{-\beta}$, and use WMAP concordant cosmology (Spergel et al., 2003) with $H_0 = 71$ km s⁻¹ Mpc⁻¹, $\Omega_M = 0.27$, and $\Omega_\Lambda = 0.73$. Uncertainties are given at 68% confidence level for one parameter of interest unless stated otherwise.

2. Observations

2.1. Photometry

In order to get a good coverage of the light curve, we obtained data using several different telescopes around the world. Our complete data set comprises 18, 2, 27, 115, 21, 13, 10 and 10 data points in *B*, *g'*, *V*, *R*, *I*, *J*, *H* and *K_S* respectively, a total of 218 points, one of the largest photometric samples of an optical/NIR afterglow in the *Swift* era.

Early optical data were obtained with the 1.5m telescope on Mt. Maidanak/Uzbekistan, the 2.6m Shajn telescope at CrAO (Crimean Astrophysical Observatory/Ukraine), the TNG (Telescopio Nazionale Galileo) on La Palma equipped with DOLores, the 1.2m MIRO telescope on Mt. Abu/India, with BFOC (Bologna Faint Object Spectrograph & Camera) at the G. D. Cassini 152 cm telescope of the Bologna University under poor conditions and with the RTT150 (1.5m Russian-Turkish telescope, Bakirlitepe, Turkey), data of the latter are also presented in Khamitov et al. (2007).

The light curve was followed up sparsely every night over nearly a week with the DFOSC (Danish Faint Object Spectrograph and Camera) on the Danish 1.54m telescope on La Silla/Chile under partially photometric conditions and with MOSCA and ALFOSC (Andalucia Faint Object Spectrograph and Camera) at the Nordic Optical Telescope on La Palma. Furthermore, two epochs were obtained with the Tautenburg 1.34m Schmidt telescope and two sets of images were taken several days after the GRB with Keck/LRIS simultaneously in the Kron-Cousins R and the Sloan g' bands, the second observation was performed at high airmass under bad seeing conditions. Late images were obtained with FORS 2 at the VLT on Paranal/Chile on Feb. 23, 2007 and Mar. 30, 2008 under the ESO-LP 177.A-059 in the R band with exposure times of 2500 and 7500s, respectively, to look for the host galaxy.

Near infrared data were collected with ANDICAM and the 1.3 m SMARTS telescope (Small and Moderate Aperture Research Telescope System) at CTIO under non-photometric conditions as well as with the robotic 1.3m PAIRITEL telescope on Mt. Hopkins.

For the photometric calibration, we determined the absolute magnitude of six comparison stars in the field using photometric zero points from DFOSC in V , R and I band (see Table 2). These stars were then used to perform relative PSF photometry to get the absolute magnitude of the afterglow, only for some of the late NOT images and the faint MIRO detections relative aperture photometry was done using a circle of 20 pixel diameter (10 for the sky). For the B -band we took zero points for only three comparison stars from the SDSS (see Table 2), converting them with the equations of Jester et al. (2005). g' zero points were taken from the SDSS. For the RTT 150 data, we used one USNO-B1 star as reference that was calibrated using Landolt standard stars. The results are in full agreement with the rest of the data set. The J , H and K band data from SMARTS/ANDICAM and PAIRITEL were calibrated using three and ten nearby stars, respectively, from the 2MASS catalogue.

All data and upper limits are given in Table 6, the data are not corrected for Galactic extinction. For the final light curve fitting, we add $Br'R_Ci'$ band data from Dai et al. (2007) and Watcher R and CR data from French et al. in prep. We shift the R band data of Dai et al. (2007) and French et al. in prep. by 0.1 magnitudes to bring it to our zero point. The multi-color light curves are shown in Fig. 1.

2.2. Spectroscopy

Spectra were obtained with FORS1/VLT on May 27 from 9 to 12 hours after the burst. Four different grisms cover the wavelength range from 3650 to 9200 Å. For all four grisms a 1''0 slit was used which provides resolving powers between 2.4 and 11.1 Å. Reduction, cosmic ray removal, extraction and wavelength calibration were performed using standard tasks in IRAF¹. The final

Table 1. Spectra of GRB 060526 from FORS1/VLT

time	exptime	grism	spectral range	resolution
May 27 [UT]	[s]		[Å]	[Å]
01:16:56	600	300V	3650 – 8900	11.1
01:29:46	900	600I	7000 – 9200	4.4
01:47:28	900	1200B	3860 – 4400	2.4
02:05:27	900	600V	4080 – 7200	4.5
02:24:00	1200	300V	3650 – 8900	11.1
02:57:05	1800	1200B	3860 – 4400	2.4
03:30:34	1800	600V	4080 – 7200	4.5
04:04:08	1800	600I	7000 – 9200	4.4

Table 2. Magnitudes of the comparison stars used for photometry

#	coord.	B	V	R	I
		[mag]	[mag]	[mag]	[mag]
1	15:31:19.6 +00:16:59.5	19.90	19.36	19.02	18.64
2	15:31:22.7 +00:17:21.2	20.30	19.51	19.09	18.71
3	15:31:20.9 +00:16:39.1	19.97	19.11	18.55	18.12
4	15:31:14.4 +00:17:49.9	—	19.78	19.43	18.81
5	15:31:16.5 +00:17:55.5	—	20.34	19.96	20.59
6	15:31:18.3 +00:18:17.7	—	20.49	19.45	18.23

spectra were then normalised as no absolute flux calibration was needed. In order to improve the S/N, we combined the datasets taken with the same grism weighted with their variance. A summary of the spectroscopic observations is given in Table 1.

2.3. The multi-color light curve

The early light curve up to two hours after the burst features an optical flare contemporaneous to the XRT/BAT flare at ≈ 250 s and a following plateau phase (Brown et al., 2006; French & Jélinek, 2006; Rykoff et al., 2006). These features will be discussed in French et al. in prep.

To analyse the evolution of the light curve, we use the R band which has the densest sampling, a total of 241 data points in all, from 2.2 hours to more than 7 days after the GRB (earlier data will be discussed in French et al. in prep. and are not included in these fits). For all fits, we fix the host magnitude to $m_h = 27$ (see § 2.7). A fit with a single power law to this data is very strongly rejected, with $\chi^2/\text{d.o.f.} = 24.3$ (see Table 3 for all fitting results). A smoothly broken power law gives a much better fit ($\Delta\chi^2 = 4943$ for three additional degrees of freedom), but even so, the fit is formally rejected, with $\chi^2/\text{d.o.f.} = 3.89$. This is due to the strong variability in the light curve which was first found by Halpern et al. (2006a) and is also discussed in Dai et al. (2007). This fit, along with the residuals showing the strong variability, is shown in Fig. 2. The parameters we find for this fit are concurrent with those of Dai et al. (2007) (who find $\alpha_1 \approx 1.0$, $\alpha_2 \approx 2.9$ and $t_b \approx 2.55$ days). Due to the high data density, we are able to let the break smoothness parameter n vary, and our result is in agreement with the tentative $\alpha_1 - n$ correlation found by Zeh et al. (2006). Still, the significant improvement shows that the light curve is basically a smoothly broken power law, and the very steep late decay indicates that this break is a jet break, as first noted by Thöne et al. (2006) and also found by Dai et al. (2007). The rest frame jet break time of 0.57 days is typical for the optical afterglows of the pre-*Swift* GRB sample (Zeh et al., 2006).

¹ <http://iraf.noao.edu>

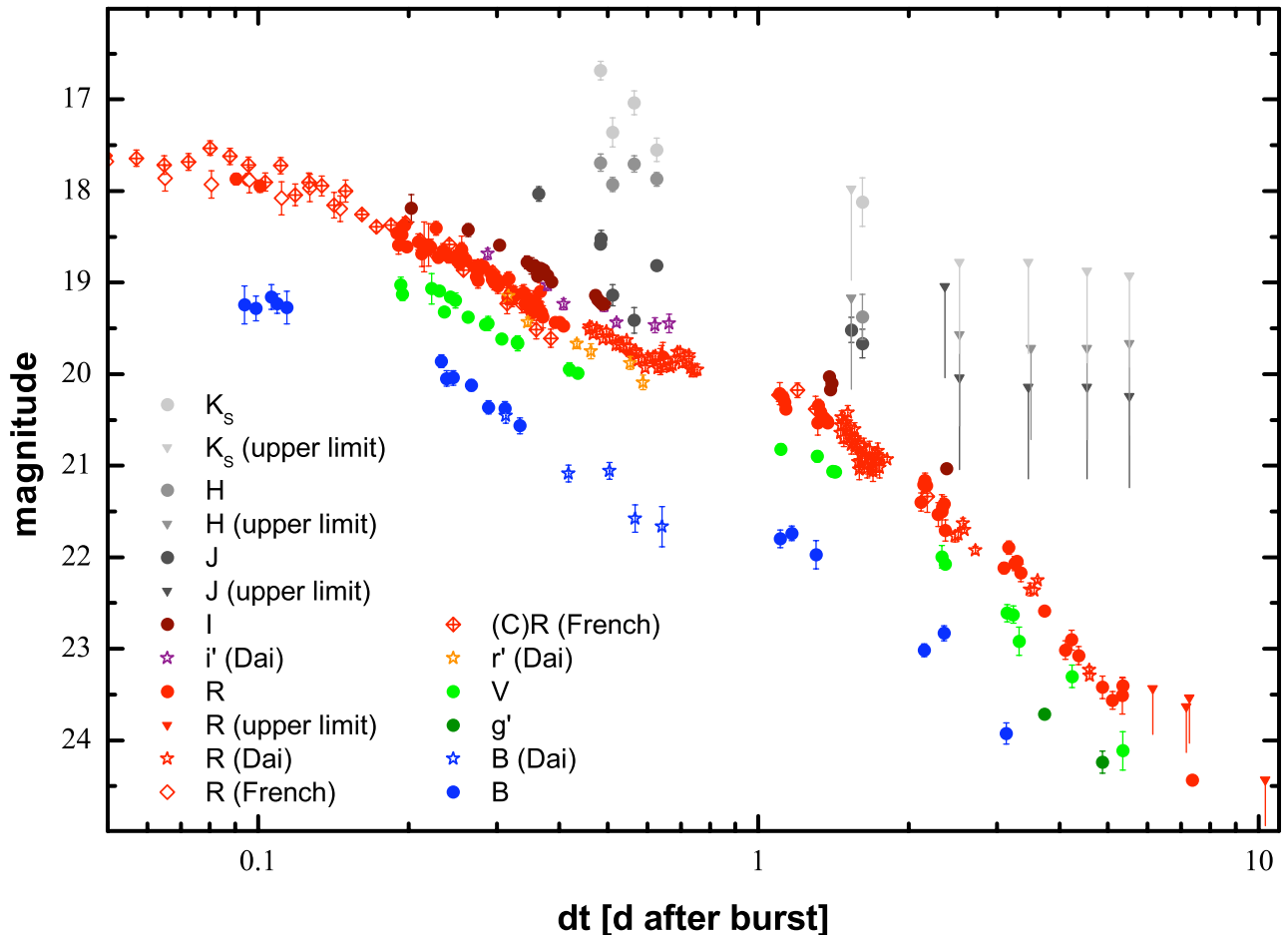


Fig. 1. Light curves of the optical afterglow of GRB 060526. Filled circles (detections, $Bg'VRIJHK_S$) and filled triangles (upper limits, $RJHK_S$) are presented in this work, open stars ($Br'Ri'$) are taken from Dai et al. (2007) and open diamonds are Watcher data from French et al. in prep. The strong variability and the large $V - R$, $B - R$ colours due to the high redshift are evident.

Jet breaks, a common feature in well-monitored pre-*Swift* optical afterglows (e.g., Zeh et al., 2006), have not been found in many *Swift* afterglows, especially in the X-rays (e.g., Mangano et al., 2007; Grupe et al., 2007; Sato et al., 2007), and if there are breaks, then the comparison between the optical and X-ray light curves show them to often be chromatic (Panaitescu et al., 2006; Oates et al., 2007). Analysing both the optical and X-ray data of GRB 060526, Dai et al. (2007) suggest that the (jet) break is achromatic. If we take the X-ray data from Dai et al. (2007) and fit it with the parameters of our smoothly broken power law fit using X-ray data from 0.06 days onward, we concur that the fit is acceptable, with $\chi^2 = 46.2$ for 39 degrees of freedom. A fit to the X-ray data alone results in a much earlier break time and slopes that are less steep (again in agreement with Dai et al., 2007), but we caution that the late X-ray afterglow is only sparsely sampled and shows large scatter. Similar results are obtained with the X-ray data as to be presented by French et al. in prep. as well as the light curve from the *Swift* XRT repository (Evans et al., 2007).

2.4. Analysis of the light curve variability

One approach to analyse the variability of the light curve is to split it into different parts and fit these with smoothly broken or single power laws. This is possible due to the high data density. The results of this approach are given in Table 3 and shown in Fig. 3. The early data from 0.08 up to 0.4 days (# 27 – 120 in

Table 3) are decently fit ($\chi^2/\text{d.o.f.} = 1.248$) by a smoothly broken power law (in all these cases, we fixed the break smoothness parameter, as it was not possible to leave it free to vary) which reveals a phase of rather steep decay early on. This situation is similar to GRB 030329, albeit less pronounced, where the steep decay of an early jet break goes over into multiple rebrightenings (Uemura et al., 2003; Zeh et al., 2006; Gorosabel et al., 2006). Such rebrightening features then follow (# 121 – 144, # 145 – 171 in Table 3), although once more less pronounced than in the case of GRB 030329. Both rebrightenings from 0.46 to 0.76 days feature a steep decay phase atypical for an external-shock driven afterglow, although we caution that the error bars are very large and it is not clear how close the derived slopes are to their hypothetical asymptotic values. The evolution of the residuals of GRB 021004 and GRB 030329 was very similar (Zeh et al., 2006), but we do not find a similar evolution in the residuals of GRB 060526 if we compare them to those of the two other GRBs.

Following a data gap, the afterglow of GRB 060526 can be modelled by a succession of single power laws which, with one exception, become successively steeper (the final five rows in Table 3). The sampling at later times is less dense, but there seem to be “steps”, phases where the afterglow remains constant for a while (or even rebrightens) before going over into a steep decay again. Such features were also seen in the afterglows of GRB 000301C (Masetti et al., 2000), GRB 021004 and GRB 030329

Table 3. Fits to the afterglow of GRB 060526. Columns are the numbering of the data points in the respective fit, the time span of these data points, the goodness of the fit, the degrees of freedom, the magnitude normalisation (see Zeh et al., 2006), the pre-break and post-break decay slopes, the break time and the smoothness of the break. The first two fits are discussed in § 2.3, all other fits in § 2.4.

#	time span (days)	χ^2	d.o.f.	m_k (mag)	α_1	α_2	t_b (days)	n
27 – 269	0.080 – 7.379	5868.3	241	20.447 ± 0.004	1.177 ± 0.004
27 – 269	0.080 – 7.379	925.82	238	21.194 ± 0.027	0.963 ± 0.007	2.759 ± 0.070	2.407 ± 0.061	3.013 ± 0.426
27 – 120	0.080 – 0.408	112.32	90	18.691 ± 0.119	0.820 ± 0.049	1.595 ± 0.121	0.257 ± 0.024	10
121 – 144	0.459 – 0.594	26.940	20	19.783 ± 0.043	1.109 ± 0.141	6.738 ± 3.588	0.585 ± 0.009	10
145 – 171	0.601 – 0.755	35.19	23	19.829 ± 0.034	-0.160 ± 0.240	7.115 ± 5.313	0.741 ± 0.012	10
172 – 185	1.093 – 1.378	14.160	12	20.172 ± 0.051	0.967 ± 0.179
186 – 206	1.461 – 1.578	26.847	19	19.737 ± 0.228	2.025 ± 0.500
207 – 235	1.585 – 1.808	23.652	27	20.614 ± 0.145	0.500 ± 0.249
236 – 250	2.114 – 2.715	23.998	13	19.184 ± 0.272	2.503 ± 0.275
251 – 268	3.168 – 5.352	93.232	16	17.930 ± 0.123	3.194 ± 0.085

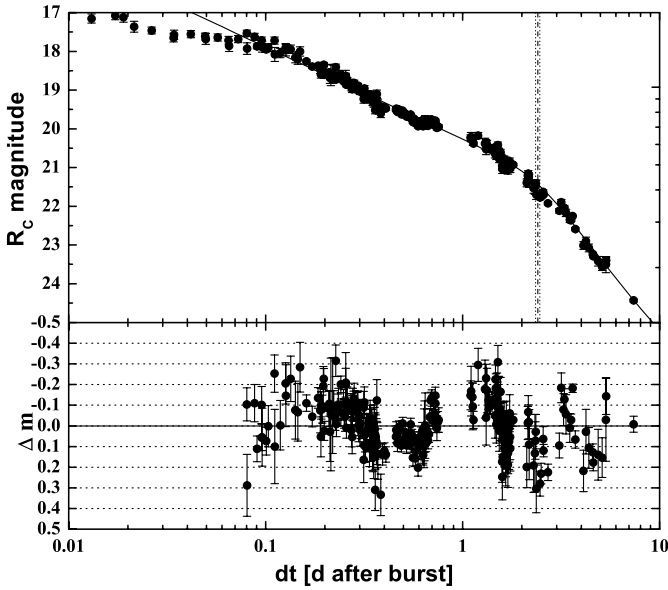


Fig. 2. The R -band light curve of GRB 060526 fit with a smoothly broken power law. The residuals of the fit show strong variations of up to 0.3 magnitudes. The dashed vertical line marks the break time, the dotted lines the 1σ region of uncertainty. Note that this is the time when the two asymptotic power-laws would meet for a maximally sharp break ($n = \infty$), in reality, the break is soft ($n \approx 3$) and is thus seen as a smooth rollover.

(e.g. Lipkin et al., 2004; Zeh et al., 2006). The decay from 3.2 to 5.4 days is very steep, $\alpha = 3.2 \pm 0.1$ (concurrent with Dai et al., 2007, who find $\alpha = 3.4 \pm 0.2$ at late times), implying an abnormally large electron power law index $p = 3.2 - 3.4$, as the post-jet break decay is $\alpha_2 = p$ in the standard fireball model. We note that all fits have $\chi^2/\text{d.o.f.} \geq 1.25$ due to scatter in the data points. It is unclear whether this scattering is due to intrinsic microvariability or to the underestimation of photometric errors. The mixing of two data sets is probably not the reason, as the data from 0.46 to 0.76 days, for example, is almost exclusively from Dai et al. (2007).

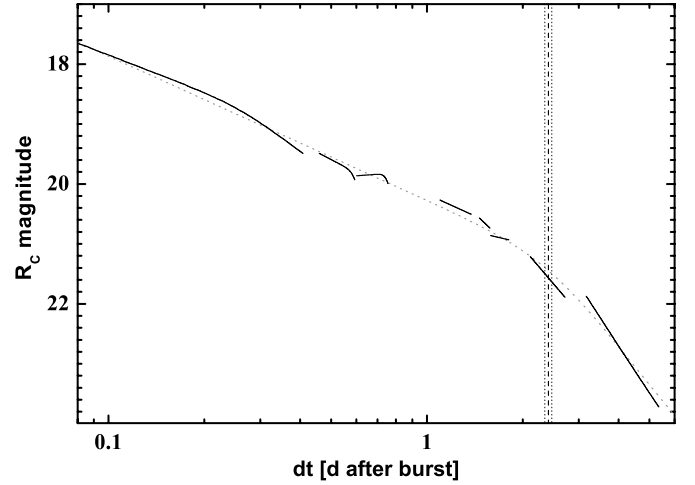


Fig. 3. Fits of the R -band light curve of GRB 060526. The gray dotted line shows the fit using a smoothly broken power law given in Fig. 2. The black lines show the fits (smoothly broken power laws or single power laws) to different parts of the light curve. The parameters can be found in Table 3. The flares at 0.5 to 0.7 days can be seen, as well as the “step” structure in the post-jet break decay.

2.5. Modelling the light curve numerically with energy injections

Motivated by the similarities to such highly variable light curves as that of the afterglow of GRB 021004, which was successfully modelled by multiple energy injections (“refreshed shocks”) (de Ugarte Postigo et al., 2005), we used the code of Jóhannesson, Björnsson & Gudmundsson (2006) to model the afterglow light curve by applying several energy injection episodes as a possible scenario to explain the rebrightenings and shallow decay of the afterglow. Figure 4 shows the best fit ($\chi^2/\text{d.o.f.} = 2.8$) found using a model with a total of six energy injections: at 0.006, 0.015, 0.04, 0.09, 0.4 and 0.6 days. The initial energy injected into the outflow is $E_0 = 5^{+3}_{-2} \cdot 10^{49}$ ergs². The energy injections then add 0.8, 1.7, 2.6, 5, 8, and finally 13 times the initial energy release E_0 to the afterglow, for a total energy release in the afterglow of $1.5^{+1.1}_{-0.7} \cdot 10^{51}$ ergs.

² The error limits presented here are 1 sigma estimates, but due to degeneracy in the model parameters, the actual range of parameter values can be much larger.

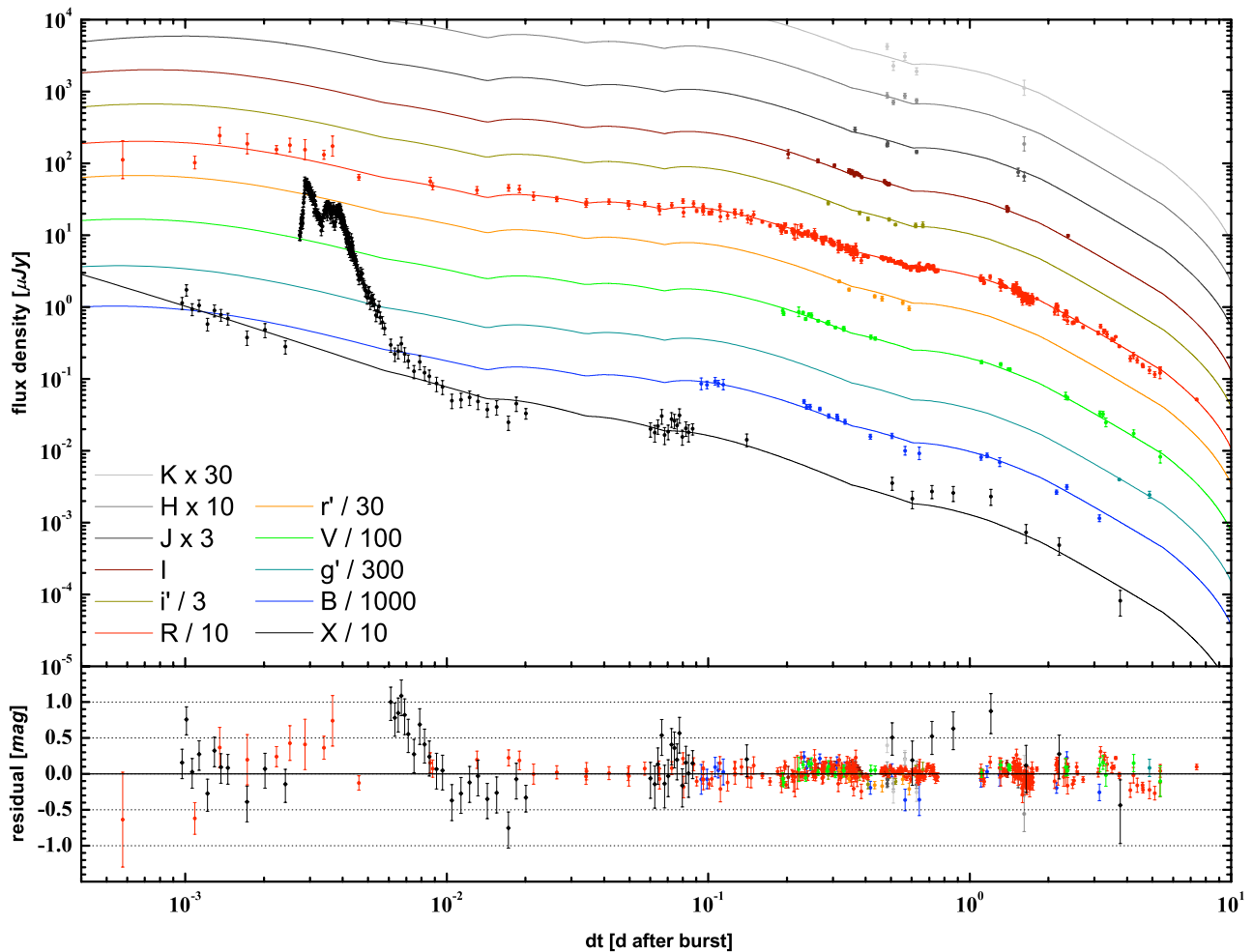


Fig. 4. Fit to the light curve in X-ray and optical/NIR $r'R'IJHK_S$ bands including a total of six energy injections. The strong X-ray flare is excluded from the modelling. The light curves have been offset by constant factors as given in the figure legend for better legibility. The $Bg'V$ bands are affected by additional Lyman forest absorption and were not included in the fit. For the $Bg'V$ bands, the fit curves the model predicts have been multiplied by 0.50, 0.55 and 0.82 respectively to match them with the data. The residuals are clearly improved in comparison to those plotted in Fig. 2, but short-timescale variations like the one at 0.7 days are still not fit satisfactorily.

The first four injections are responsible for the shallow afterglow decay between 0.008 and 0.25 days. The quality of the data does not allow to discriminate between this four-injection scenario and a continuous injection (French et al. in prep.). Also, since there are no direct indications of injections in the light curve, the time of each of the four injections is not well determined. A direct consequence of this is that the energy of each individual injection in this phase is not well determined, while the total energy released is fairly consistent. The time and energy of the last two injections are, however, better constrained by the data.

Further results of the modelling are a high density of the circumburst medium of $n_0 = 250^{+500}_{-150} \text{ cm}^{-3}$ (a high value, comparable to the high- z GRB 050904, Frail et al., 2006), a rather low opening angle of $\theta_0 = 1^{\circ.5^{+1.9}_{-0.8}}$ and an electron index of $p = 2.1^{+0.3}_{-0.1}$. The peak frequency ν_m passes through the optical/NIR at very early times (French et al. in prep.), explaining the optical peak, and the cooling break ν_c is between the optical and X-rays up to 6 days after the burst, i.e., over the whole data span. Furthermore, we find $\varepsilon_e = 2 \cdot 10^{-2}$ and $\varepsilon_B = 8^{+40}_{-6} \cdot 10^{-5}$, with ε_e being the fraction of the energy in the electron popula-

tion and ε_B the fraction of the energy in the magnetic field. Note that the definition of ε_e has been changed in the model from Jóhannesson, Björnsson & Gudmundsson (2006) to the definition of Panaitescu & Kumar (2001) to allow for $p < 2$ in the model. In addition, we defined a maximum Lorentz factor for the electron energy distribution. This is limited by both synchrotron cooling (Dai & Lu, 1998) and, when $p < 2$, energy conservation (Panaitescu & Kumar, 2001). The steep decay at around 6 days is due to this restriction on the electron energy distribution, where the emission is cut off above the synchrotron frequency associated with this Lorentz factor. This interpretation is sensitive to the value assumed for the maximum Lorentz factor, which in turn is not well known. We have also assumed that the electron distribution is abruptly cut off at the maximum Lorentz factor, but a steepening at that point has also been suggested (e.g. Panaitescu & Kumar, 2001). Data at later times are needed to discriminate between the two and confirm this explanation for the steep decay.

This model reproduces the optical/NIR light curves well, with the rather high $\chi^2/\text{d.o.f.} = 2.8$ resulting from the inability to fit the microvariability of the afterglow. We excluded both

Table 4. Fits to the spectral energy distribution of GRB 060526. Columns are the dust model, the goodness of the fit, the spectral slope and the derived extinction in the rest-frame V band.

dust	$\chi^2/\text{d.o.f.}$	β	A_V
none	0.054	0.663 ± 0.025	...
MW	0.062	0.691 ± 0.044	-0.038 ± 0.048
LMC	0.052	0.327 ± 0.323	0.163 ± 0.156
SMC	0.048	0.495 ± 0.144	0.049 ± 0.041

V and B bands from the fit due to Lyman forest blanketing. The X-ray light curve is also fitted reasonably well, but the model underpredicts the X-ray flux after the last energy injection and does not fall as steeply as the data. Here, the powerful X-ray flare has not been included in the fit, as it most likely originates in an internal shock caused by late time central engine activity (e.g., Burrows et al., 2005).

2.6. The spectral energy distribution and host extinction

Following the procedures outlined in Kann et al. (2006), we derive the optical spectral energy distribution (SED) of the GRB 060526 afterglow and fit it with several dust models (Milky Way (MW), Large (LMC) and Small Magellanic Clouds (SMC), Pei, 1992) to derive the line-of-sight extinction in the host galaxy. Due to the strongly variable light curve, we choose the approach Kann et al. (2006) used for the SED of GRB 030329, and shift the other bands to the R band zero point to derive the colours. With this method, we can also look for colour changes. There may be marginal variations in $B - R$, but this colour remains constant within conservative errors.

The $Bg'Vr'R_Ci'I_CJHK_S$ SED clearly shows the decreasing flux in the B , g' and V bands due to the Lyman forest blanketing (see Fig. 5), and we thus do not include these filters in our fit. Due to the conservative errors, all fits, even with no extinction, are acceptable (see Table 4) and we are thus unable to strongly prefer one dust model over another. Furthermore, the extinction found is consistent with being zero in all cases, similar to the results for several other high redshift *Swift* GRBs (Kann et al., 2007). The MW and LMC extinction laws are disfavoured, as they result in unphysical negative extinction and a too flat spectral slope, respectively. The lack of z band data does not allow us to constrain the existence of a 2175 \AA bump. Thus, we henceforth use the SMC dust fit, again in accordance with pre-*Swift* (Kann et al., 2006; Starling et al., 2007) and *Swift*-era (Schady et al., 2007; Kann et al., 2007) results. Assuming the cooling break ν_c to lie blueward of the optical bands (highly likely considering the X-ray spectral slope $\beta_X \approx 1$, Dai et al., 2007, French et al., in prep.; and the result of the numerical modelling), the standard fireball model gives for the electron power law index $p = 2\beta + 1 = 1.99 \pm 0.29$. This result is in agreement with the result from the broadband modelling (§ 2.5) and with the canonical $p = 2.2$, and very similar to many other GRB afterglows (e.g. Kann et al., 2006). On the other hand, it does not agree with $p = 3.2 \pm 0.1$ from the late optical decay. Our results are in contrast to Dai et al. (2007), who derive a very steep slope $\beta_0 = 1.69^{+0.53}_{-0.49}$ from $Br'i'$ data only (correcting for Lyman absorption) and conclude that the optical and the X-ray data lie on the same slope.

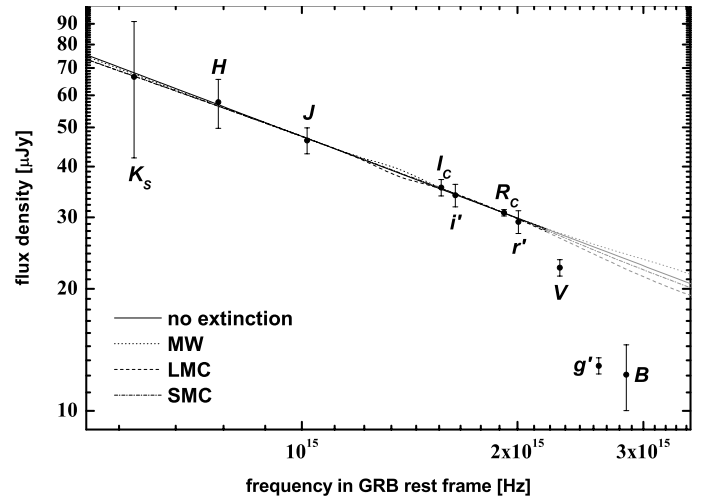


Fig. 5. Spectral energy distribution of the afterglow of GRB 060526 in $Bg'Vr'R_Ci'I_CJHK_S$, and fits with no extinction (straight black line), MW extinction (dotted line), LMC extinction (dashed line) and SMC extinction (thick dash-dotted line). Data beyond $2.2 \times 10^{15} \text{ Hz}$ ($Vg'B$) were not included in the fit due to Lyman forest blanketing, the grey curves represent extrapolations. The flux density scale is measured at the break time of 2.4 days.

2.7. Host search

In the VLT images, we do not detect any source at the position of the afterglow down to a limit of $R = 27.1 \text{ mag}$ (which transforms into an absolute magnitude limit of $M_R = -20.1$), see Fig. 6 for an image of the field. However, there are two sources present, the first one $\sim 1''$ South-East of the afterglow position with $R = 26.4 \pm 0.2$, the second one $\sim 1''.5$ North-West with $R = 26.3 \pm 0.2$, which at a redshift of $z = 3.221$ would transform into physical distances of ~ 7.7 and 11.5 kpc . A longslit spectrum covering the afterglow position and the source close to the GRB site does not show any trace at these positions, however, collapsing the entire spectrum blue- and redward of Lyman- α at the redshift of the burst respectively and plotting the two values along the slit gives a small enhancement near the source to the South-East (Milvang-Jensen et al. in prep). If this detection is significant, it gives a lower limit for the source of $z > 3.221$ and makes this source likely to be the host of GRB 060526. We note, however, that this would be one of the largest offsets found between a GRB and its host galaxy in a large sample of *Swift* long GRB host galaxies (Hjorth et al. in prep.).

Host galaxies of long-duration GRBs have been found to often be faint irregular galaxies (Fruchter et al., 2006; Christensen et al., 2004) which are difficult to detect at higher redshifts. So far, there are only five bursts with $z > 3$ where the detection of a host galaxy has been published, namely GRB 971214 ($z = 3.42$) (Kulkarni et al., 1998), GRB000131 ($z = 4.5$) (Fruchter et al., 2006), GRB 030323 (Vreeswijk et al., 2004), GRB 060206 ($z = 4.047$) (Thöne et al., 2008) and GRB 060605 ($z = 3.773$) (Ferrero et al., 2008). The host galaxies of GRB 020124 (Berger et al., 2002) and GRB 050904 (Berger et al., 2007), on the other hand, were not detected to very deep limits.

The distribution of pre-*Swift* R band host galaxy magnitudes peaks at $M_{AB} = 25$ (Fruchter et al., 2006) but extends out to 29 with a typical redshift $z \approx 1.4$. *Swift* GRBs (and thus their hosts) however have a higher mean redshift of $z = 2.8$ (Jakobsson et al., 2006a), so the distribution will be shifted out to even fainter

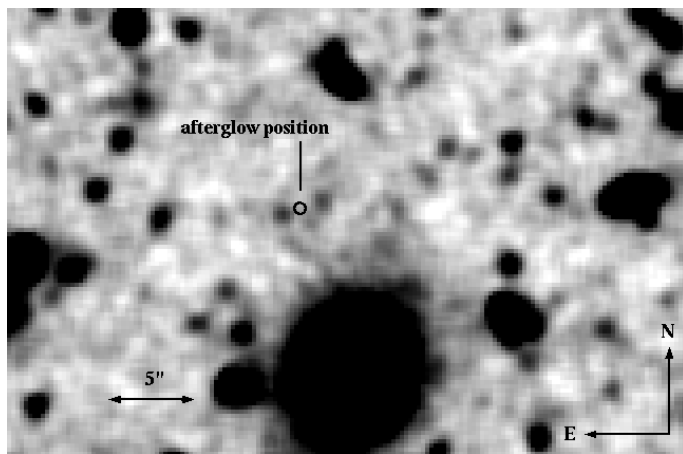


Fig. 6. *R* band image of the field of GRB 060526. The afterglow position is indicated and no source is detected at that position. The image has been smoothed to enhance weak sources.

magnitudes. Ovoldsen et al. (2007) also find a higher magnitude for *Swift* hosts than for pre-*Swift* bursts by comparing the expected detection rate from pre-*Swift* hosts with detections and upper limits derived from imaging the fields of 24 *Swift* and *HETE* bursts from 2005 – 2006. If the source close to the GRB position is indeed the host galaxy of GRB 060526, it would be among the more luminous hosts detected for long-duration GRBs.

3. Spectroscopy results

3.1. Line identification

We detect a range of metal absorption lines as well as a Lyman limit system (LLS) originating in the host galaxy of GRB 060526. A redshift of $z=3.221$ was determined in Jakobsson et al. (2006b) from a number of these absorption lines using the spectra taken with the 600V grism presented in this article.

Most of the lines were fitted from the combined 600V spectrum which covers all metal absorption lines detected longwards of Ly- α , but provides a higher resolution than the 300V spectra. The 600I spectra only covers the AlIII λ 1670 line at the same resolution as the 600V grism. The range of 1200B is entirely within the Lyman- α forest but does not have a high enough resolution to deblend metal transitions from absorption caused by the Ly- α forest lines. We do, however, detect Ly- β and Ly- γ absorption in the 1200B grism. In the blue end of the 300V spectrum, one can clearly see the 915 Å Lyman break at the redshift of the host galaxy. In Fig. 7, we show the combined spectrum of the 300V grism with the identified lines indicated.

In order to determine the equivalent width (EW) of strong absorption lines, we fitted the continuum around the lines in regions that were free of absorption and summed over the absorption contained within two times the full-width at half-maximum (FWHM) of the lines. For weak lines, we obtained better results due to the low S/N by fitting Gaussians. For this fit, we used a modified version of the gaussfit procedure provided in IDL³ which is more reliable in determining the continuum and fitting the actual line even if it is slightly blended with a neighbouring line. The upper limits on the EWs for a range of ions noted in Table 3.1 was determined from the spectra taken with the 300V grism due to the better S/N of those spectra.

³ available at <http://www.pa.iasf.cnr.it/~nicastro/IDL/Lib/gfit.pro>

Table 5. EWs of detected absorption lines and 2σ upper limits on some undetected lines, the EW for the blended systems include the contributions from all lines. The column densities were derived from CoG fitted for S II, Si II, Fe II and C IV. Upper and lower limits were determined by assuming the ions to lie on the linear part of the CoG. The Ly α column density is taken from Jakobsson et al. (2006b) and is based on the 600V grism.

λ_{obs} [Å]	λ_{rest} [Å]	id	z	EW _{rest} [Å]	log N [cm ⁻²]
4102.26	972.54	Ly γ	3.218	2.39±0.10	—
4329.70	1025.72	Ly β	3.221	2.92±0.06	—
5131	1215.67	Ly α	3.221	—	20.01±0.15
(5254)	1242.80	N V	(3.221)	<0.05	<13.66
(5276)	1250.58	S II	(3.221)	<0.04	<14.71
5291.01	1253.81	S II	3.220	0.05±0.02	14.58±0.25
5320.00	1259.52	S II	3.221	(1.32±0.07)	—
	1260.42	Si II	3.221	<i>blended</i>	>13.89
	1260.53	Fe II	3.221	—	—
(5335)	1264.74	Si II*	(3.221)	<0.09	<12.76
5497.30	1302.17	O I	3.222	1.07±0.06	>15.15
5506.82	1304.37	Si II	3.222	0.70±0.21	>14.72
(5559)	1317.22	Ni II	(3.221)	<0.09	<13.59
5634.24	1334.53	C II	3.222	(1.51±0.22)	—
	1335.71	C II	3.222	<i>blended</i>	—
5884.87	1393.76	Si IV	3.222	0.20±0.08	13.50±0.14
5923.05	1402.77	Si IV	3.222	0.12±0.05	13.50±0.14
6444.50	1526.71	Si II	3.221	0.86±0.04	>14.48
6539.58	1548.20	C IV	3.223	0.26±0.08	14.10±0.13
6546.39	1550.78	C IV	3.221	0.22±0.09	14.10±0.13
6790.24	1608.45	Fe II	3.221	0.17±0.03	14.28±0.24
6800.38	1611.20	Fe II	3.221	<0.01	—
7052.62	1670.79	Al II	3.221	1.02±0.05	>13.34
(7829)	1854.72	Al III	(3.221)	<0.09	<12.71
(8552)	2026.13	Zn II	(3.221)	<0.10	<12.73
(8679)	2056.25	Cr II	(3.221)	<0.12	<13.47

S II λ 1259, Si II λ 1260 and Fe II λ 1260 are blended and cannot be fitted separately, the same is the case for C II $\lambda\lambda$ 1334, 1335. We therefore cannot consider them for the derivation of the column density from the curve of growth fit as described below and only give the total EW Table 3.1. In contrast to what is noted in Jakobsson et al. (2006b), we cannot reliably detect any fine-structure lines and only give an upper limit for Si II*. Fine structure lines would be a clear indication that the absorption lines detected are indeed originating in the host galaxy of the GRB (e.g. Prochaska et al., 2006; Vreeswijk et al., 2007). The redshift derived is therefore strictly taken only as a lower limit. Investigating the individual, uncombined spectra we could not detect any variability in the EW which is most likely due to the relatively low S/N of the individual spectra.

3.2. Column densities from curve of growth analysis

Some of the strong absorption lines are saturated, which is a problem in low resolution spectra as the damping wings are not resolved and Voigt profile (VP) fitting cannot be adopted to derive a reliable column density. Furthermore, high resolution spectra of GRBs (Prochaska, 2006) have shown that the strong metal absorption lines unresolved in low resolution spectra usually consist of a number of narrow, unsaturated components that would allow an accurate determination of the column density by fitting the different components separately.

If only low resolution spectra are available, one has to adopt a curve of growth (CoG) analysis (Spitzer, 1978) which directly

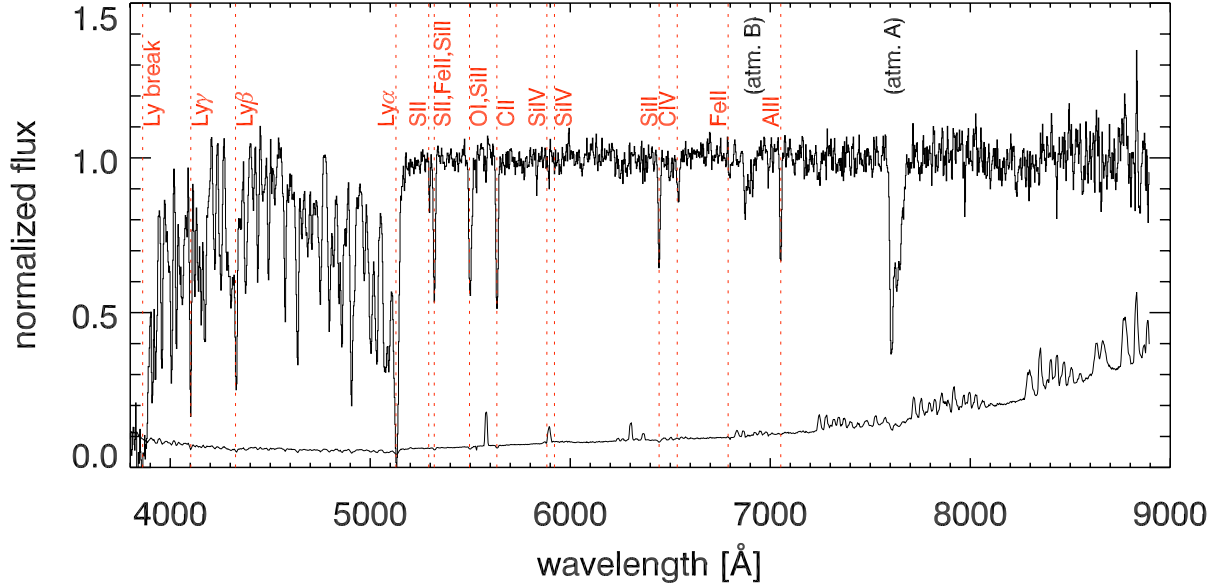


Fig. 7. The spectrum taken with grism 300V where the two exposures have been combined to improve the S/N. The identified lines are labelled as well as the main atmospheric absorption bands. The line at the bottom shows the error spectrum.

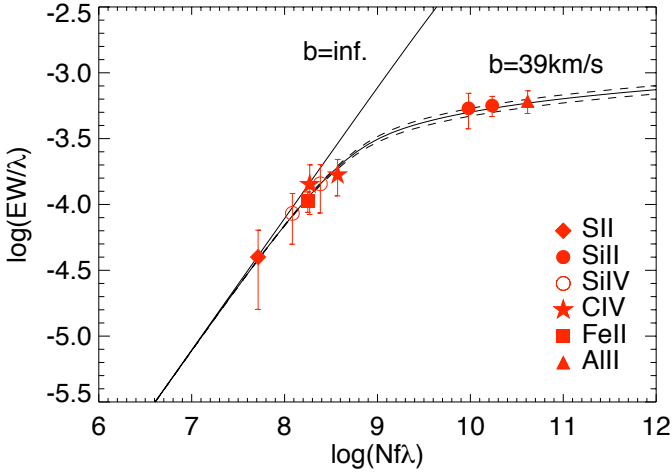


Fig. 8. Multi-ion single-component curve of growth fit for the absorption systems in GRB 060526 using 6 different ions. As comparison, $b = \infty$ is plotted, the dotted line marks the 1σ deviation from the fit

relates the EW to the column density on the linear part of the CoG where the lines are not saturated (optical depth $\tau_0 < 1$), but depends on the Doppler b parameter of the medium on the flat part of the curve which applies for mildly saturated lines. For GRBs, one usually has to do a multiple-ion single-component CoG (MISC-CoG) analysis, adopting the same effective Doppler parameter for all ions. Here, we used all unblended ionic lines that were not heavily saturated, namely S II, Si II, Fe II, Al II as well as C IV and Si IV and calculate the χ^2 minimum going through the parameter space for the column densities of each ion and a range of b parameters. We then find the best fit for $b = 39 \pm 3 \text{ km s}^{-1}$ (see Fig. 8) and the column densities as noted in Table 3.1. Most of the ions lie near the linear part of the CoG and are therefore rather independent of b , Si II and Al II lie on the flat part of the CoG and the column densities are only noted as lower limits as derived from the linear part of the CoG.

We excluded the saturated O I transition from the fit as well as Si II λ 1260 which is blended with S II and Fe II where, however, Si II is the dominant contribution.

There are several problems connected with the use of the CoG that have to be considered. Different ionisation levels should actually be treated in separate analyses as they might occur in different regions in the absorbing system. However, we assume that the absorption takes place in a relatively small region of the host galaxy and also fit the higher ionisation levels of Si IV and C IV in the same CoG. Furthermore, they lie on the linear part of the CoG and excluding them from the common fit would not change the derived b parameter. Another problem with doing multiple-ion CoG analysis using strong lines in low-resolution spectra has been noted by Prochaska (2006), who compared column densities derived from low resolution spectra and CoG with high resolution data and VP fitting from the same bursts. He found that when including saturated lines in the fit, column densities are generally underestimated. Indications for that are if an effective b parameter of $\gg 20 \text{ km s}^{-1}$ is found as strong lines actually consist of a range of components with $b < 20 \text{ km s}^{-1}$ and that weak lines are underestimated when including saturated lines in the CoG. Savaglio (2006) however performed a similar analysis using CoG and the apparent optical depth (AOD) method as described in Pettini et al. (2002) which can be applied for medium resolution high S/N spectra and found a good agreement between the two methods. We also find that the column densities of the saturated lines Al II and Si II are quite sensitive to the adopted b parameter. These lines consist very likely of a number of unresolved weaker components which would lie on the linear part of the CoG. For Al II and Si II we therefore give the column density derived from the linear part of the CoG as lower limit.

3.3. Metallicity and relative abundances

Absorption lines that are likely not affected by dust extinction can be used to derive a metallicity of the medium in the line of sight to the GRB. The least dust-depleted element is Zn, which is, however, undetected in our spectra. We there-

fore use S II, Fe II and the strongest lower limit on Si II to derive relative metallicities compared to the hydrogen density with $[M/H] = \log(N_M/N_H) - \log(N_M/N_H)_\odot$ using solar abundances from Asplund, Grevesse & Sauval (2005). Here we derive metallicities of $[S/H] = -0.57 \pm 0.25$, $[Si/H] > -0.80$ and $[Fe/H] = -1.18 \pm 0.24$.

Fe is usually affected by dust depletion (Savage & Sembach, 1996) and corrections have to be adopted. Using the relation between the Zn and Fe abundance in Savaglio (2006), we find a metallicity of $[Fe/H] = -1.09 \pm 0.24$ which marginally agrees within the errors with the value derived from sulphur. The only detected and unblended S II line at λ 1253, however, is only marginally detected and therefore the EW has large errors. The Fe II doublet taken for the CoG fit, in contrast, is also slightly blended, but the fit of the stronger component can be considered as reliable. Despite the dust depletion, the metallicity derived from Fe might be the most reliable one in this case and we therefore assume a metallicity of $[Fe/H] = -1.09$ for the host of GRB 060526.

Independent of the ion used for the metallicity, it is rather high compared to other galaxies at redshift $z \approx 3$, but among the typical metallicities derived for other GRB hosts (Fynbo et al., 2006) at that redshift. For those measurements, different ions have been used depending on the quality and the wavelength coverage of the spectra. Our results show that caution is required when comparing the metallicities derived from different elements, as they might be differently affected by dust extinction and/or evolution. This is especially true when saturated lines in low resolution spectra are used to derive the column densities and hence the abundances as it is the case for, e.g., GRB 000926 (Savaglio et al., 2003) and GRB 011211 (Vreeswijk et al., 2006). For GRB 050401 (Watson et al., 2006) and GRB 050505 (Berger et al., 2005), the authors themselves note that due to saturation the metallicity is indeed a lower limit.

Our spectra do not allow us to determine a dust depletion pattern from the relative abundances of heavier elements, since at least four elements such as Zn, Si, Mn, Cr, Fe, Ni or S are necessary. However, the difference in the relative abundances between S, Si and Fe suggest the presence of some dust in the line-of-sight towards the GRB. On the other hand, this difference could also be due to an enhancement in α element production⁴ which is likely to happen in the young star-forming host of a GRB. Generally, GRB hosts have higher α/Fe ratios than QSO-DLAs (Prochaska et al., 2007), which can either be interpreted as large dust depletion consistent with the higher metallicities of GRB sightlines or as α element enhancement. There are indications that most of the α/Fe ratio is due to dust depletion traced by a large $[Zn/Fe]$ or $[Ti/Fe] < 0$. The latter is assumed to be a clear indicator of dust depletion ($[Ti/Fe] < 0$) vs. α enhancement ($[Ti/Fe] > 0$) (Dessauges-Zavadsky et al., 2002). Both elements are, however, not detected and the limit on Zn does not lead to a strong constraint on the $[Zn/Fe]$ ratio to settle this issue in the case of GRB 060526.

We do not detect NV in our spectra but provide an upper limit of $\log N < 13.66$. NV was detected in only four sightlines towards GRBs (Prochaska et al., 2008) and likely traces the immediate environment of the GRB as it has a high ionization potential and requires a strong radiation field. Our upper limit is lower than the column densities for those GRB sightlines where NV could be detected which implies that the ab-

sorbing gas probed by our spectra are most likely not close to the GRB itself. Furthermore, we do not detect any fine structure lines and only derive an upper limit on Si II* of $\log N < 12.76$. Fine structure lines are assumed to be pumped by the UV radiation field of the GRB (Vreeswijk et al., 2007) which also indicates that the gas is likely very far from the GRB itself. Si II* requires a less strong radiation field and has been detected in Lyman Break Galaxies (Pettini et al., 2002) where the UV radiation from young stars provides the necessary radiation field. Our tentative host also has a large offset from the GRB and the gas in the sightline is therefore expected to be little affected by UV radiation from young stars in the host.

4. Discussion and conclusions

GRB 060526 had a relatively bright afterglow that allowed us to obtain a solid dataset, both photometrically and spectroscopically. We achieved a dense light curve coverage over several days which allowed a detailed study of the afterglow properties, and obtained a series of low resolution but high signal-to-noise spectra to study the host environment.

4.1. A highly variable light curve

The optical light curve can be fitted with a broken power-law with a break at $t_b = 2.401 \pm 0.061$ days and decay slopes of $\alpha_1 = 0.963 \pm 0.007$ and $\alpha_2 = 2.759 \pm 0.070$ before and after the break. The dense sampling of especially the *R* band light curve also reveals a number of variabilities on top of the broken power-law resembling what has been seen in a GRB 021004 (de Ugarte Postigo et al., 2005) and GRB 030329 (Lipkin et al., 2004).

These features could be explained either by extended activity of the central engine or through interactions of the shock with the interstellar medium. For the case that the variability arises from external shocks, several mechanisms have been considered. In GRB 021004, both density variations of the external medium into which the GRB jet plows and angular inhomogeneities of the jet surface were considered (Nakar et al., 2003). However, Nakar & Granot (2007) show that density variations would cause much smaller fluctuations than those observed in GRB afterglows and can therefore be ruled out. Another possibility is the injection of additional energy into the shock by slower shells that catch up with the shocked region as it decelerates, this model was used successfully to describe GRB 021004 (de Ugarte Postigo et al., 2005) and also works better than two other models (double jet and density fluctuations) to describe the highly complex light curve of GRB 030329 (Huang et al., 2006). Thus, variability can give either information on the medium surrounding the GRB or on the activity of the central engine. A more intriguing possibility is that the flares may be emitted from another region closer to the central engine, resulting from late internal shocks. Powerful X-ray flares that are attributed to late central engine activity have been observed in about 50% of all *Swift* GRBs (e.g. Burrows et al., 2005; Chincarini et al., 2007; Krimm et al., 2007), and strong optical/NIR flaring contemporaneous with the GRB prompt emission may also occur (Vestrand et al., 2005; Blake et al., 2005; Vestrand et al., 2006; Racusin et al., 2008), thus making optical flares from late central engine activity an interesting prospect (Kann, 2007; Malesani et al., 2007).

Indeed, Dai et al. (2007) have suggested that the optical variability of the afterglow of GRB 060526 is due to flares from late internal shocks. Khamitov et al. (2007) conclude that the short timescale of the variabilities requires the jet to be non-relativistic already at ~ 1 day and could then be explained by

⁴ α elements are produced in massive, metal-poor stars through the α process and include elements with integer multiples of the He nucleus mass such as O, Si, S, Ca, Mg and Ti.

external density fluctuations. Our analysis lends tentative support to the notion of flares from internal shocks, finding decay slopes for two flares that exceed what should be possible from external shocks. But we caution that the errors of these fits are large due to a low amount of data in the decaying parts. Furthermore, globally, a model using refreshed external shocks is able to account for the light curve variations, although microvariability remains. This creates the intriguing possibility of reverberation effects (see Vestrand et al., 2006, for a case of reverberation between gamma-rays and optical emission). Short flares in the X-ray or optical bands signal internal shocks from long-term central engine activity, and when these shells catch up with the forward shock front, they re-energise the external forward shock. The detection of such behaviour would probably require dense multi-band observations of a bright afterglow to search for SED changes at high time resolution combined with detailed modelling of the data. This way, one could discern between internal shocks (which are expected to have a different spectral index from the forward shock afterglow) and refreshed, external shocks (which are achromatic). Our data set of the afterglow of GRB 060526, while extensive and exemplary for the *Swift* era, does not allow us such a detailed decomposition.

4.2. A moderate metallicity environment

From the analysis of our low resolution spectra with different resolutions, we detect a LLS and a number of metal absorption lines that all lie at a redshift of $z=3.221$. The low resolution only allows us to derive column densities from measuring the EWs of the absorption lines and adopt a MISC-CoG analysis where we exclude the most saturated as well as blended transitions. We find a best fit for the Doppler parameter of $b=39\pm 3.0$ km⁻² and most of the ions used for the fit lie on the linear part of the CoG which allows a reliable determination of the column densities. The relative abundances of different metals in the spectra indicate some dust extinction, but an intrinsic difference due to enhancement of the production of certain elements cannot be excluded. The very low amount of dust detected in the afterglow SED may indicate that the latter might be the favored possibility.

We derive a metallicity for the host of $[Fe/H] = -1.09$ which is slightly higher than metallicities determined from other GRB afterglow spectra. According to the definition of QSO absorbers, the host of GRB 060526 is classified as a LLS ($19 < \log N_{HI} < 20.3$) which seem to have on average higher metallicities than Damped Lyman Alpha systems (DLAs) (Poux et al., 2007) and a steeper evolution towards lower redshifts. Around redshift 3, however, the metallicities of both samples are within the same range. Also, GRB hosts show a trend towards increasing metallicity with lower redshifts (Fynbo et al., 2006; Savaglio, 2006). Taking into account that most of the sample used only low-resolution spectra to derive the metallicity (which only gives lower limits for the column densities and the metallicity) this evolution might, however, not be as pronounced as for DLAs and LLS. This might imply that the enrichment of the ISM in the early universe had taken place at earlier times than assumed.

There is a possible detection of a host galaxy with $R = 26.4 \pm 0.2$ at a large offset of 7.7 kpc from the afterglow position, which would make it a rather luminous host, if the source is indeed connected to the GRB. GRBs are assumed to trace the star-formation history of the universe and star formation is assumed to shift towards smaller and fainter galaxies over time as massive galaxies prove to be rather unchanged throughout the history of the universe (e.g. Abraham et al., 1999; Heavens et al., 2004). One would therefore expect that GRB hosts should

also have higher luminosities towards higher redshifts. Fynbo et al. (2008) concluded that the observed metallicity distribution of GRB hosts (as well as QSO absorbers) at $z\approx 3$ can be explained by the luminosity function of galaxies at that redshift and assuming a luminosity-metallicity relation as derived for other high redshift samples (Ledoux et al., 2006; Erb et al., 2006). GRBs are then assumed to reside in higher luminosity galaxies compared to QSO-DLAs which would match with the tentative host detection for GRB 060526.

Acknowledgements. CCT wants to thank Cédric Ledoux for comments on the curve-of-growth analysis. We thank the support astronomer and staff at the Nordic Optical Telescope for obtaining the observations.

The Dark Cosmology Centre is funded by the DNRF. HD acknowledges support from the Research Council of Norway. PJ acknowledges support by a Marie Curie Intra-European Fellowship within the 6th European Community Framework Program under contract number MEIF-CT-2006-042001, and a Grant of Excellence from the Icelandic Research Fund. PAC gratefully acknowledges the support of NWO under grant 639.043.302. CB, AG, and GG acknowledge the University of Bologna for the funds Progetti di Ricerca Pluriennali.

Based on observations made with the Nordic Optical Telescope, operated on the island of La Palma jointly by Denmark, Finland, Iceland, Norway, and Sweden, with the William Herschel Telescope and the Telescopio Nazionale Galileo in the Spanish Observatorio del Roque de los Muchachos of the Instituto de Astrofísica de Canarias and at the Astronomical Observatory of Bologna in Loiano (Italy). Collection of SMARTS data is supported by NSF-AST 0707627. MIRO is supported by the Department of Space, Govt. of India. The Peters Automated Infrared Imaging Telescope (PAIRITEL) is operated by the Smithsonian Astrophysical Observatory (SAO) and was made possible by a grant from the Harvard University Milton Fund, the camera loan from the University of Virginia, and the continued support of the SAO and UC Berkeley. The PAIRITEL project and JSB are further supported by NASA/Swift Guest Investigator Grant NNG06GH50G. We thank M. Skrutskie for his continued support of the PAIRITEL project. The W.M. Keck Observatory is operated as a scientific partnership among the California Institute of Technology, the University of California and the National Aeronautics and Space Administration and was made possible by the generous financial support of the W.M. Keck Foundation.

References

- Abraham, R. G., Ellis, R. S., Fabian, A. C., Tanvir, N. R. & Glazebrook, K., 1999, *MNRAS*, 303, 641
- Antonelli, L. A., Testa, V., Romano, P., et al. 2006, *A&A*, 456, 509
- Asplund, M., Grevesse, N., Sauval, A. J. 2005, *Cosmic Abundances as Records of Stellar Evolution and Nucleosynthesis in honor of David L. Lambert*, ASP Conference Series, Vol. 336, Proceedings of a symposium held 17-19 June, 2004 in Austin, Texas. Edited by Thomas G. Barnes III and Frank N. Bash. San Francisco: Astronomical Society of the Pacific, 2005., p.25
- Berger, E., & Gladders, M. 2006, *GCN* 5170
- Berger, E., Kulkarni, S. R., Bloom, J. S., et al. 2002, *ApJ*, 581, 981
- Berger, E., Penprase, B. E., Cenko, S. B., et al. 2005, *ApJ*, submitted (astro-ph/0511498)
- Berger, E., Chary, R., Cowie, L. L., et al. 2007, *ApJ*, 665, 102
- Beuermann, K., Hessman, F. V., Reinsch, K., et al. 1999, *A&A*, 352, L26
- Blake, C. H., Bloom, J. S., Starr, D. L., et al. 2005, *Nature*, 435, 181
- Brown, P. J., Campana, S., Boyd, P. T., & Marshall, F. E. 2006, *GCN* 5172
- Burrows, D. N., Romano, P., Falcone, A., et al., 2005, *Science*, 309, 1833
- Campana, S., Barthelmy, S. D., Boyd, P. T., et al. 2006a, *GCN* 5162
- Campana, S., Barthelmy, S. D., Burrows, D. N., et al. 2006b, *GCN* 5163
- Campana, S., Moretti, A., Guidorzi, C., Chincarini, G., Burrows, D. N. 2006c, *GCN* 5168
- Chincarini, G., Moretti, A., Romano, P., et al. 2007, *ApJ*, 671, 1903
- Christensen, L., Hjorth, J., & Gorosabel, J. 2004, *A&A*, 425, 913
- Covino, S., D'Avanzo, P., Klotz, A., et al. 2008, *MNRAS*, in press (arXiv:0804.4367)
- Dai, Z. G., Lu, T. 1998, *MNRAS*, 298, 87
- Dai, X., Halpern, J. P., Morgan, N. D., et al. 2007, *ApJ*, 658, 509
- Dessauges-Zavadsky, M., Prochaska, J. X., & D'Odoric, S. 2002, *A&A*, 391, 801
- Erb, D. K., Shapley, E. A., & Pettini, M. 2006, *ApJ*, 644, 813
- Evans, P. A., Beardmore, A. P., Page, K. L., et al. 2007, *A&A*, 469, 379
- Ferrero, P., Klose, S., Kann, D. A., et al. 2008, *A&A*, submitted (arXiv:0804.2457)
- Le Floch, E., Duc, P.-A., Mirabel, I. F., et al. 2003, *A&A*, 400, 499
- Frail, D. A., Cameron, P. B., Kasliwal, M., et al. 2006, *ApJ*, 646, L99

- French, J., & Jélinek, M. 2006, GCN 5165
- Fruchter, A. S., Levan, A. J., Strolger, L., et al. 2006, *Nature*, 441, 463
- Fynbo, J. P. U., Starling, R. L. C., Ledoux, C., et al. 2006, *A&A*, 451, L47
- Fynbo, J. P. U., Prochaska, J. X., Sommer-Larsen, J., Dessauges-Zavadsky, M., & Møller, P. 2008, *ApJ*, in press (arXiv:0801.3273)
- Garnavich, P. M., Loeb, A., & Stanek, K. Z. 2000, *ApJ*, 544, L11
- Gehrels, N., Chincarini, G., Giommi, P., et al. 2004, *ApJ*, 611, 1005
- Gorosabel, J., Castro-Tirado, A. J., Ramirez-Ruiz, E., et al. 2006, *ApJ*, 641, L13
- Grupe, D., Gronwall, C., Wang, X.-Y., et al. 2007, *ApJ*, 662, 443
- Guidorzi, C., Monfardini, A., Gomboc, A., et al. 2005, *ApJ*, 630, L121
- Guidorzi, C., Vergani, S. D., Sazonov, S., et al. 2007, *A&A*, 474, 793
- Halpern, J. P., Armstrong, E., & Mirabal, N. 2006a, GCN 5176
- Halpern, J. P., Armstrong, E., & Mirabal, N. 2006b, GCN 5188
- Heavens, A., Panter, B., Jimenez, R., & Dunlop, J. 2004, *Nature*, 428, 625
- Huang, Y. F., Cheng, K. S., & Gao, T. 2006, *ApJ*, 637, 873
- Jakobsson, P., Hjorth, J., Ramirez-Ruiz, E., et al. 2004, *New Astron.*, 9, 435
- Jakobsson, P., Levan, L., Fynbo, J. P. U., et al. 2006, *A&A*, 447, 897
- Jakobsson, P., Fynbo, J. P. U., Ledoux, C., et al. 2006, *A&A*, 460, L13
- Jester, S., Schneider, D. P., Richards, G. T., et al. 2005, *AJ*, 130, 873
- Jóhannesson, G., Björnsson, G., & Gudmundsson, E. H. 2006, *ApJ*, 647, 123
- Kann, D. A. 2007, GCN 6209
- Kann, D. A., Klose, S., & Zeh, A. 2006, *ApJ*, 641, 993
- Kann, D. A., Klose, S., Zhang, B., et al. 2007, *ApJ*, submitted (arXiv:0712.2186)
- Khamitov, I. M., Burenin, R. A., Bikmaev, I. F. et al. 2007, *Astron. Letters*, 33, 797 (arXiv:0802.1635)
- Klose, S., Greiner, J., Rau, A., et al. 2004, *AJ*, 128, 1942
- Krimm, H. A., Granot, J., Marshall, F., et al. 2007, *ApJ*, 665, 554
- Kulkarni, S. R., Djorgovski, S. G., Ramaprakash, A. N., et al. 1998, *Nature*, 393, 35
- Laursen, L. T., & Stanek, K. Z. 2003, *ApJ*, 597, L107
- Ledoux, C., Petitjean, P., Fynbo, J. P. U., Møller, P., & Srinand, R. 2006, *A&A*, 457, 71
- Lipkin, Y. M., Ofek, E. O., Gal-Yam, A., et al. 2004, *ApJ*, 606, 381
- Malesani, D., Covino, S., D'Avanzo, P., et al. 2007, *A&A*, 473, 77
- Mangano, V., La Parola, V., Cusumano, G., et al. 2007, *ApJ*, 654, 403
- Markwardt, C., Barbier, L., Barthelmy, S. D., et al. 2006, GCN 5174
- Masetti, N., Bartolini, c., Bernabei, S., et al. 2000, *A&A*, 359, L23
- Mészáros, P. 2006, *Rep. Prog. Phys.*, 69, 2259
- Molinari, E., Vergani, S. D., Malesani, D., et al. 2007, *A&A*, 469, L13
- Monfardini, A., Kobayashi, S., Guidorzi, C., et al. 2006, *ApJ*, 648, 1125
- Mundell, C. G., Melandri, A., Guidorzi, C., et al. 2004, *ApJ*, 660, 489
- Nakar, E., Piran, T., & Granot, J. 2003, *New Astron.*, 8, 495
- Nakar, E., & Granot, J. 2007, *MNRAS*, 380, 1744
- Nysewander, M., Reichart, D. E., Crain, J. A., et al. 2007, *ApJ*, submitted (arXiv:0708.3444)
- Oates, S. R., de Pasquale, M., Page, M. J., et al. 2007, *MNRAS*, 380, 270
- Ovaldsen, J.-E., Jaunsen, A. O., Fynbo, J. P. U., et al. 2007, *ApJ*, 662, 294
- Panaiteescu, A., & Kumar, P. 2001, *ApJ*, 554, 667
- Panaiteescu, A., Mészáros, P., Burrows, D., et al. 2006, *MNRAS*, 369, 2059
- Pei, Y. C. 1992, *ApJ*, 395, 130
- Peroux, C., Dessauges-Zavadsky, M., D'Odorico, S., Kim, T.-S., & McMahon, R. G. 2007, *MNRAS*, 382, 177
- Pettini, M., Rix, A. S., Steidel, C. C., et al. 2002, *ApJ*, 569, 742
- Perley, D. A., Bloom, J. S., Butler, N. R., et al. 2008, *ApJ*, 672, 449
- Perley, D. A., Li, W., Chornock, R., et al. 2008, *ApJ*, submitted (arXiv:0805.2394)
- Piran, T. 2004, *Rev. Mod. Phys.*, 76, 1143
- Price, P. A., Songaila, A., Cowie, L. L., et al. 2007, *ApJ*, 663, L57
- Prochaska, J. X. 2006, *ApJ*, 650, 272
- Prochaska, J. X., Chen, H.-W., & Bloom, J. S. 2006, *ApJ*, 648, 95
- Prochaska, J. X., Chen, H.-W., Dessauges-Zavadsky, M., & Bloom, J. S. 2007, *ApJ*, 666, 267
- Prochaska, J. X., Dessauges-Zavadsky, M., Ramirez-Ruiz, E. & Chen, H.-W. 2008, *ApJ* in press, preprint: astro-ph/0806.0399
- Racusin, J. L., Karpov, S. V., Sokolowski, M., et al. 2008, *Nature*, submitted (arXiv:0805.1557)
- Rykoff, E. S., Yost, S. A., Swan, H., & Rujopakarn, W. 2006, GCN 5166
- Sari, R., Piran, T. & Narayan, R. 1998, *ApJ*, 497, L17
- Sato, G., Yamazaki, R., Ioka, K., et al. 2007, *ApJ*, 657, 359
- Savaglio, S., Fall, S. M., & Fiore, F. 2003, *ApJ*, 585, 638
- Savaglio, S. 2006, *New Journal of Physics*, 8, 195
- Savage, B. D., & Sembach, K. R. 1996, *ARA&A*, 34, 279
- Schady, P., Mason, K. O., Page, M. J., et al. 2007, *MNRAS*, 377, 273
- Spergel, D. N., Verde, L., Peiris, H. V., et al. 2003, *ApJS*, 148, 175
- Spitzer, L. 1978, "Physical processes in the interstellar medium", book
- Stanek, K. Z., Garnavich, P. M., Nutzman, P. A., et al. 2005, *ApJ*, 626, L5
- Stanek, K. Z., Dai, X., Prieto, J. L., et al. 2007, *ApJ*, 654, L21
- Starling, R. L. C., Wijers, R. A. M. J., Wiersema, K. et al. 2007, *ApJ*, 661, 787
- Thöne, C. C., Fynbo, J. P. U., & Jørgensen, U. G. 2006, GCN 5179
- Thöne, C. C., Greiner, J., Savaglio, S., & Jehin, E. 2007, *ApJ*, 671, 628
- Thöne, C. C., Wiersema, K., Ledoux, C., et al. 2008, *A&A*, in press (arXiv:0708.3448)
- Uemura, M., Taichi, K., Ishioka, R., et al. 2003, *Nature*, 423, 843
- de Ugarte Postigo, A., Castro-Tirado, A. J., Gorosabel, J., et al. 2005, *A&A*, 443, 841
- Updike, A. C., Haislip, J. B., Nysewander, M. C., et al. 2008, *ApJ*, in press (arXiv:0805.1094)
- Vestrand, W. T., Woźniak, P. R., Wren, J. A., et al. 2005, *Nature*, 435, 178
- Vestrand, W. T., Wren, J. A., Woźniak, P. R., et al. 2006, *Nature*, 442, 172
- Vreeswijk, P. M., Ellison, S. L., Ledoux, C., et al. 2004, *A&A*, 419, 927
- Vreeswijk, P. M., Smette, A., Fruchter, A. S., et al. 2006, *A&A*, 447, 145
- Vreeswijk, P. M., Ledoux, C., Smette, A., et al. 2007, *A&A*, 468, 83
- Watson, D., Fynbo, J. P. U., Ledoux, C., et al. 2006, *ApJ*, 652, 1011
- Waxman, E., & Draine, B. T. 2000, *ApJ*, 537, 796
- Woosley, S. E., & Heger, A. 2006, *ApJ*, 637, 914
- Woźniak, P. R., Vestrand, W. T., Wren, J. A., et al. 2006, *ApJ*, 642, L99
- Zeh, A., Klose, S., & Kann, D. A. 2006, *ApJ*, 637, 889
- Zhang, B. 2007, *ChJAA*, 7, 1

Table 6. Broad band observations of GRB 060526, times given are the midpoint of the observations. Data have not been corrected for Galactic extinction.

Δt [d]	exptime [s]	instrument	filter	mag	error
0.09394	180	Maidanak	B	19.518	0.207
0.09898	180	Maidanak	B	19.557	0.135
0.10625	180	Maidanak	B	19.432	0.136
0.10925	180	Maidanak	B	19.505	0.107
0.11421	900	Maidanak	B	19.546	0.179
0.23242	100	RTT150	B	20.133	0.069
0.23813	100	RTT150	B	20.321	0.083
0.24525	100	RTT150	B	20.316	0.081
0.26704	300	RTT150	B	20.395	0.064
0.28883	300	RTT150	B	20.636	0.074
0.31108	300	RTT150	B	20.649	0.073
0.33371	300	RTT150	B	20.839	0.085
1.10542	900	RTT150	B	22.072	0.097
1.16521	900	Maidanak	B	22.013	0.079
1.30279	900	RTT150	B	22.246	0.154
2.14626	2880	Maidanak	B	23.290	0.072
2.35104	900	MOSCA	B	23.104	0.082
3.13135	2700	Maidanak	B	24.198	0.115
3.73439	660	LRIS	g'	23.952	0.022
4.87114	660	LRIS	g'	24.480	0.120
0.19284	60	DOLORES	V	19.235	0.087
0.19443	60	DOLORES	V	19.338	0.065
0.22210	120	MIRO	V	19.274	0.167
0.23067	100	RTT150	V	19.302	0.046
0.23583	100	RTT150	V	19.527	0.047
0.24254	100	RTT150	V	19.364	0.045
0.24818	1200	BFOSC	V	19.403	0.081
0.26313	300	RTT150	V	19.584	0.040
0.28487	300	RTT150	V	19.669	0.040
0.28809	1200	BFOSC	V	19.655	0.078
0.30667	300	RTT150	V	19.821	0.040
0.32942	300	RTT150	V	19.861	0.048
0.33005	1200	BFOSC	V	19.870	0.083
0.41910	600	DFOSC	V	20.155	0.073
0.43507	600	DFOSC	V	20.200	0.057
1.10946	900	RTT150	V	21.027	0.055
1.31288	900	RTT150	V	21.105	0.060
1.40937	600	DFOSC	V	21.267	0.037
1.41685	600	DFOSC	V	21.273	0.040
1.42464	600	DFOSC	V	21.276	0.038
2.32642	900	RTT150	V	22.203	0.123
2.36561	600	DFOSC	V	22.279	0.062
3.14483	3000	RTT150	V	22.818	0.094
3.23404	3000	RTT150	V	22.834	0.094
3.32054	3000	RTT150	V	23.123	0.154
4.24058	7200	RTT150	V	23.508	0.121
5.35387	8400	RTT150	V	24.322	0.211
0.09030	180	Maidanak	R	18.039	0.062
0.09539	180	Maidanak	R	18.042	0.064
0.10079	180	Maidanak	R	18.117	0.067
0.18919	60	DOLORES	R	18.627	0.109
0.19079	60	DOLORES	R	18.763	0.097
0.19165	180	MIRO	R	18.616	0.066
0.19390	180	MIRO	R	18.646	0.068
0.19615	180	MIRO	R	18.546	0.094
0.19838	180	MIRO	R	18.775	0.046
0.20914	600	BFOSC	R	18.723	0.087
0.21225	180	MIRO	R	18.851	0.143
0.21449	180	MIRO	R	18.778	0.273
0.21897	180	MIRO	R	18.756	0.232
0.22144	900	BFOSC	R	18.779	0.083
0.22679	150	RTT150	R	18.576	0.076
0.22892	150	RTT150	R	18.892	0.061
0.23417	150	RTT150	R	18.831	0.060
0.23428	900	BFOSC	R	18.821	0.078
0.24058	150	RTT150	R	18.888	0.066
0.24829	150	RTT150	R	18.881	0.071
0.25054	150	RTT150	R	18.935	0.071
0.25279	150	RTT150	R	18.960	0.070
0.25504	150	RTT150	R	18.805	0.070
0.25530	180	MIRO	R	18.815	0.155
0.25729	150	RTT150	R	18.910	0.071
0.25954	150	RTT150	R	18.917	0.073
0.27050	150	RTT150	R	18.994	0.075
0.27275	150	RTT150	R	19.105	0.081
0.27468	900	BFOSC	R	19.017	0.074
0.27500	150	RTT150	R	19.147	0.081
0.27721	150	RTT150	R	18.993	0.074
0.27946	150	RTT150	R	19.014	0.073
0.28171	150	RTT150	R	18.986	0.075
0.29208	150	RTT150	R	19.073	0.080
0.29438	150	RTT150	R	19.131	0.081
0.29662	150	RTT150	R	19.170	0.079
0.29888	150	RTT150	R	19.129	0.077
0.30113	150	RTT150	R	19.206	0.079
0.30342	150	RTT150	R	19.183	0.074
0.31462	150	RTT150	R	19.144	0.078
0.31599	900	BFOSC	R	19.332	0.080
0.31692	150	RTT150	R	19.128	0.075
0.31917	150	RTT150	R	19.292	0.082
0.32142	150	RTT150	R	19.349	0.083
0.32371	150	RTT150	R	19.289	0.087
0.32596	150	RTT150	R	19.303	0.088
0.33725	150	RTT150	R	19.290	0.083
0.33950	150	RTT150	R	19.275	0.086
0.34179	150	RTT150	R	19.402	0.089
0.34404	150	RTT150	R	19.336	0.089
0.34629	150	RTT150	R	19.341	0.089
0.34854	150	RTT150	R	19.454	0.101
0.35083	150	RTT150	R	19.466	0.103
0.35308	150	RTT150	R	19.505	0.104
0.35533	150	RTT150	R	19.364	0.105
0.35758	150	RTT150	R	19.383	0.106
0.35983	150	RTT150	R	19.417	0.106
0.36208	150	RTT150	R	19.434	0.107
0.36433	150	RTT150	R	19.462	0.111
0.36658	150	RTT150	R	19.270	0.101
0.36883	150	RTT150	R	19.492	0.109
0.37108	150	RTT150	R	19.542	0.122
0.39230	600	DFOSC	R	19.603	0.051
0.40064	600	DFOSC	R	19.607	0.039
0.40800	600	DFOSC	R	19.644	0.037
0.53319	600	DFOSC	R	19.820	0.044
0.54030	600	DFOSC	R	19.868	0.041
0.54841	600	DFOSC	R	19.899	0.042
0.62960	600	DFOSC	R	20.058	0.090
0.63685	300	DFOSC	R	20.030	0.142
0.64096	300	DFOSC	R	20.001	0.145
0.64468	300	DFOSC	R	19.982	0.158
1.10432	540	Shajn 2.6m	R	20.382	0.120
1.11983	900	RTT150	R	20.426	0.069
1.12784	540	Shajn 2.6m	R	20.478	0.113
1.13576	1080	Maidanak	R	20.551	0.041
1.31530	900	BFOSC	R	20.700	0.133
1.31725	900	RTT150	R	20.512	0.068
1.33046	900	BFOSC	R	20.582	0.108

dt [d]	exptime [s]	instrument	filter	mag	error	dt [d]	exptime[s]	instrument	filter	mag	error
1.35328	600	DFOSC	R	20.648	0.043	0.36436	360	ANDICAM	J	18.090	0.080
1.36091	600	DFOSC	R	20.668	0.040	0.48350	1177	PAIRITEL	J	18.638	0.054
1.37108	600	DFOSC	R	20.686	0.042	0.48494	360	ANDICAM	J	18.580	0.090
1.37829	600	DFOSC	R	20.699	0.038	0.51112	2260	PAIRITEL	J	19.196	0.114
1.49769	600	DFOSC	R	20.864	0.038	0.56496	683	PAIRITEL	J	19.472	0.141
1.50549	600	DFOSC	R	20.836	0.039	0.62604	2190	PAIRITEL	J	18.872	0.054
1.51330	600	DFOSC	R	20.871	0.037	1.53323	706	PAIRITEL	J	19.575	0.138
1.60597	600	DFOSC	R	20.954	0.047	1.61412	2237	PAIRITEL	J	19.725	0.157
1.61369	600	DFOSC	R	21.031	0.059	2.36277	360	ANDICAM	J	>19.1	
1.62117	600	DFOSC	R	20.986	0.067	2.52278	2237	PAIRITEL	J	>20.1	
2.11423	1260	Maidanak	R	21.565	0.100	3.46425	2213	PAIRITEL	J	>20.2	
2.14083	900	RTT150	R	21.373	0.080	4.50410	2266	PAIRITEL	J	>20.3	
2.15346	900	RTT150	R	21.330	0.080	5.52048	2260	PAIRITEL	J	>20.3	
2.16637	900	RTT150	R	21.389	0.082	0.48350	1177	PAIRITEL	H	17.726	0.095
2.29040	2400	TLS 1.34m	R	21.700	0.130	0.51112	2260	PAIRITEL	H	17.963	0.077
2.32674	900	MOSCA	R	21.671	0.188	0.56496	683	PAIRITEL	H	17.741	0.089
2.33858	900	RTT150	R	21.619	0.091	0.62604	2190	PAIRITEL	H	17.908	0.074
2.35204	900	RTT150	R	21.587	0.083	1.53323	706	PAIRITEL	H	>19.2	
2.36504	900	RTT150	R	21.875	0.115	1.61412	2237	PAIRITEL	H	19.410	0.244
3.10104	1800	Maidanak	R	22.286	0.060	2.52278	2237	PAIRITEL	H	>19.6	
3.16792	3000	RTT150	R	22.062	0.072	3.50562	2237	PAIRITEL	H	>19.8	
3.25538	3000	RTT150	R	22.239	0.077	4.54525	2260	PAIRITEL	H	>19.8	
3.28438	1800	MOSCA	R	22.213	0.052	5.52048	2260	PAIRITEL	H	>19.7	
3.34992	3000	RTT150	R	22.338	0.095	0.48350	1177	PAIRITEL	K _S	16.710	0.101
3.73440	660	LRIS	R	22.758	0.042	0.51112	2260	PAIRITEL	K _S	17.385	0.159
4.11354	2700	Maidanak	R	23.181	0.100	0.56496	683	PAIRITEL	K _S	17.062	0.132
4.23200	7200	RTT150	R	23.072	0.108	0.62604	2190	PAIRITEL	K _S	17.576	0.128
4.37326	1800	MOSCA	R	23.244	0.099	1.53323	706	PAIRITEL	K _S	>18.0	
4.87336	900	LRIS	R	23.587	0.123	1.61412	2237	PAIRITEL	K _S	18.148	0.265
5.10382	3420	Maidanak	R	23.733	0.096	2.52278	2237	PAIRITEL	K _S	>18.8	
5.34483	9000	RTT150	R	23.680	0.201	3.46425	2213	PAIRITEL	K _S	>18.8	
5.35173	3600	ALFOSC	R	23.571	0.088	4.54525	2260	PAIRITEL	K _S	>18.9	
6.14534	3420	Maidanak	R	>23.6		5.52048	2260	PAIRITEL	K _S	>19.0	
7.17834	3600	Maidanak	R	>23.8							
7.26820	12000	TLS 1.34m	R	>23.7							
7.37882	3600	ALFOSC	R	24.602	0.039						
10.3198	3600	ALFOSC	R	>24.6							
272.654	2500	FORS2	R	>27.1							
672.332	7500	FORS2	R	(combined)							
0.20221	180	MIRO	I	18.311	0.149						
0.26296	900	BFOSC	I	18.549	0.070						
0.30365	900	BFOSC	I	18.715	0.055						
0.34481	900	BFOSC	I	18.901	0.070						
0.35175	360	ANDICAM	I	18.940	0.090						
0.35683	360	ANDICAM	I	18.937	0.062						
0.36191	360	ANDICAM	I	19.052	0.056						
0.36692	360	ANDICAM	I	18.967	0.043						
0.37107	600	DFOSC	I	19.009	0.048						
0.37200	360	ANDICAM	I	18.987	0.036						
0.37888	600	DFOSC	I	19.050	0.045						
0.38632	600	DFOSC	I	19.118	0.042						
0.47240	360	ANDICAM	I	19.266	0.059						
0.47737	360	ANDICAM	I	19.310	0.050						
0.48238	360	ANDICAM	I	19.338	0.052						
0.48747	360	ANDICAM	I	19.361	0.060						
0.49254	360	ANDICAM	I	19.359	0.048						
1.38701	600	DFOSC	I	20.152	0.039						
1.39420	600	DFOSC	I	20.294	0.042						
1.40178	600	DFOSC	I	20.223	0.049						
2.37793	900	MOSCA	I	21.156	0.041						